JOURNAL OF GEOPHYSICAL RESEARCH, VOL. 111, C10008, doi:10.1029/2005JC003302, 2006

Radar imaging mechanism of marine sand waves at very low grazing angle illumination caused by unique hydrodynamic interactions

Ingo Hennings[1] and Dagmar Herbers[1]

Received 20 September 2005; revised 20 April 2006; accepted 29 June 2006; published 20 October 2006.

[1] The investigations carried out between 2002 and 2004 during six field experiments within the Operational Radar and Optical Mapping in monitoring hydrodynamic, morphodynamic and environmental parameters for coastal management (OROMA) project aimed to improve the effectiveness of new remote sensing monitoring technologies such as shipborne imaging radars in coastal waters. The coastal monitoring radar of the GKSS Research Center, Geesthacht, Germany, is based on a Kelvin Hughes RSR 1000 X band (9.42 GHz) vertical (VV) polarized river radar and was mounted on board the research vessel *Ludwig Prandtl* during the experiments in the Lister Tief, a tidal inlet of the German Bight in the North Sea. The important progress realized in this investigation is the availability of calibrated X band radar data. Another central point of the study is to demonstrate the applicability of the quasi-specular scattering theory in combination with the weak hydrodynamic interaction theory for the radar imaging mechanism of the seabed. Radar data have been taken at very low grazing angles $\leq 2.6°$ of flood and ebb tide–oriented sand wave signatures at the sea surface during ebb tidal current phases. Current speeds perpendicular to the sand wave crest ≤ 0.6 m s^{-1} have been measured at wind speeds ≤ 4.5 m s^{-1} and water depths ≤ 25 m. The difference between the maximum measured and simulated normalized radar cross section (NRCS) modulation of the ebb tide–oriented sand wave is 27%. For the flood tide–oriented sand wave, a difference of 21% has been calculated. The difference between the minimum measured and simulated NRCS modulation of the ebb tide–oriented sand wave is 10%, and for the flood tide–oriented sand wave, a value of 43% has been derived. Phases of measured and simulated NRCS modulations correspond to asymmetric sand wave slopes. The results of the simulated NRCS modulation show the qualitative trend but do not always quantitatively match the measured NRCS modulation profiles because the quasi-specular scattering theory at very low grazing angle is a first-order theory.

Citation: Hennings, I., and D. Herbers (2006), Radar imaging mechanism of marine sand waves at very low grazing angle illumination caused by unique hydrodynamic interactions, *J. Geophys. Res.*, *111*, C10008, doi:10.1029/2005JC003302.

1. Introduction

[2] Signatures of normalized radar cross section (NRCS) modulation at the ocean surface due to sea bottom topography are visible on a variety of radar images derived by shore- and ship-based radar as well as by real aperture radar (RAR) and synthetic aperture radar (SAR) on board airborne and spaceborne platforms [*McLeish et al.*, 1981; *Hennings et al.*, 1994; *Vogelzang et al.*, 1997; *Lamont-Smith et al.*, 2005]. A first descriptive explanation of such phenomena was given by *De Loor* [1981] and coworkers in the Netherlands. They had noticed surface manifestations of marine sand waves in coastal waters in K_a band airborne radar imagery acquired on 19 September 1969, one hour before low tide at the Dutch coast of the southern North Sea. SEASAT, the first satellite specifically designed to study the oceans, was launched in 1978. The SEASAT L band SAR recorded spectacular images of bottom topography in coastal seas <50 m water depth like the Great Bahama Bank Southern Edge Tongue of the Ocean, the southern North Sea, the English Channel, the Thames Estuary, the Irish Sea, the Bristol Channel, and the Nantucket Shoals [*Alpers and Hennings*, 1984; *Shuchman et al.*, 1985]. These bathymetric features stimulated many research activities because the radar imaging mechanism of such phenomena has been not well understood at that time. Theoretical models of the radar imaging mechanism of sea bottom topography have been described and discussed by *Alpers and Hennings* [1984], *Phillips* [1984], *Shuchman et al.* [1985], *Zimmerman* [1985], *Hennings* [1990], *Romeiser and Alpers* [1997], and *Vogelzang* [1997].

[1]Leibniz-Institut für Meereswissenschaften an der Universität Kiel, Kiel, Germany.

0148-0227/06/2005JC003302$09.00

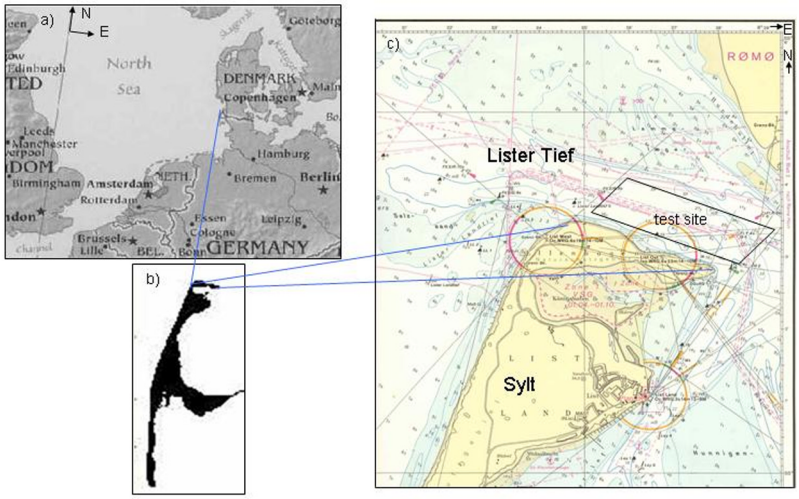

Figure 1. (a and b) Locations of the island of Sylt and the Lister Tief in the German Bight of the North Sea. (c) Bathymetry of the Lister Tief tidal channel bounded by the islands of Sylt to the south and Rømø to the north. The OROMA experiments have been carried out in the sea area of the Lister Tief marked by the parallelogram.

[3] An overview of general spatial scales of bed forms and ocean floor topography as a function of water depth by using different remote sensing radar systems was presented by *Hennings* [1998]. Imaging radars are used for the detection of tidal current ridges, sand waves, and other morphological changes of the seafloor in water depths $\leq$50 m. The private company ARGOSS, in the Netherlands, has improved their depth monitoring system based on the two-dimensional version of the Bathymetry Assessment System (BAS-2D) for mapping water depths of shallow coastal waters using SAR and echo sounding data [*Hesselmans et al.*, 2000; *Calkoen et al.*, 2001]. *Inglada and Garello* [2002] presented a technique by rewriting classical physical models as a series of nonlinear filters using Volterra models. They demonstrated by using such a technique that the inversion algorithm avoids the use of an iterative data assimilation scheme. Their method is based only on the physical knowledge of the imaging mechanism which is expressed by the so-called Volterra kernels.

[4] Many advances in understanding the radar imaging mechanism of marine sand waves have been realized within the field experiment of the C-STAR project in the southern North Sea using an airborne SAR and a special buoy system [*Hennings et al.*, 2001]. However, the study of radar signatures in coastal waters described by *Donato et al.* [1997] also demonstrated the critical nature that topographic and stratified effects could have via the associated hydrodynamics for the interpretation of radar imagery. *Li et al.* [1999] presented radar signatures of internal waves superimposed on surface manifestations caused by the seabed. The influence of quasi-resonant internal waves on the radar imaging mechanism of shallow sea bottom topography was discussed by *Hennings et al.* [2002]. The question if the water column in any coastal area is vertically well mixed and stratification can be neglected when discussing the NRCS modulation caused by the seafloor has to be carefully investigated, too. Other oceanographic phenomena like frontal boundaries, small-scale eddies, slicks, oil spills, patches of turbulence and ship wakes are quite common in coastal waters and can disturb as well the radar signatures of the seabed.

[5] The aim of this paper is to investigate if the quasi-specular scattering theory can be applied at very low grazing angle illumination to explain the X band radar imaging mechanism of marine sand waves caused by unique hydrodynamic interactions.

[6] The experiment and measurement configuration are presented in section 2. In section 3 the seabed morphology of the Lister Tief is described. Acoustic Doppler current profiler (ADCP) measurements and the characteristic fluid flow associated with macroturbulence related to marine sand waves are discussed in section 4. The shipborne radar data including their calibration procedure of the Lister Tief are shown in section 5. The quasi-specular scattering theory is presented in section 6. Simulated and measured NRCS modulation data caused by marine sand waves are compared in section 7. Finally, section 8 contains the discussion and conclusions.

2. Experiment and Measurement Configuration

[7] Six field experiments of the Operational Radar and Optical Mapping in monitoring hydrodynamic, morphodynamic and environmental parameters for coastal management (OROMA) project of the Fifth Framework Programme of the European Commission (EC) have been carried out between 2002 and 2004. The study area is the Lister Tief, a tidal inlet of the German Bight in the North Sea bounded by the islands of Sylt to the south and Rømø to the north, respectively, as shown in Figures 1a–1c. The OROMA experiments took place in the sea area of the Lister Tief marked by the parallelogram in Figure 1c. The measurements performed on board the research vessel (R/V) *Ludwig Prandtl* of the GKSS Research Center, Geesthacht, Germany, will be described here.

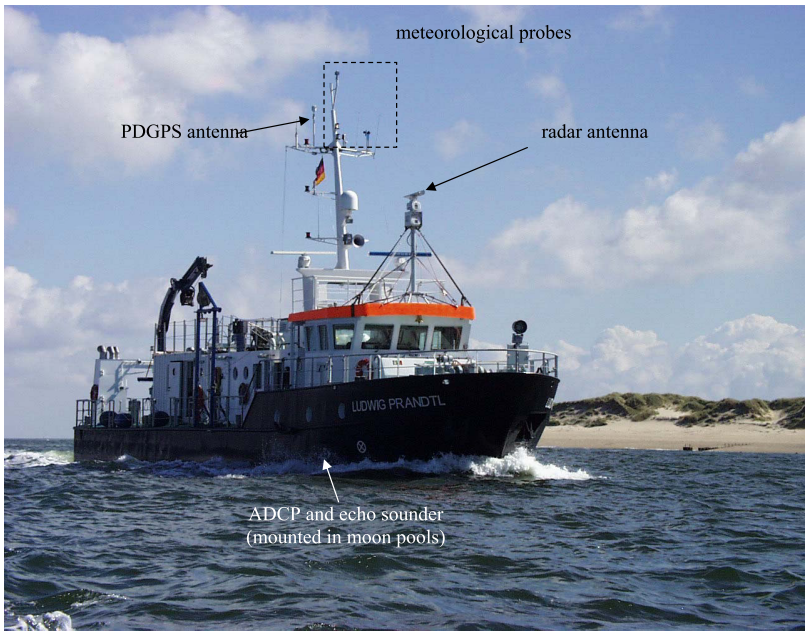

Figure 2. Measurement configuration on board research vessel (R/V) *Ludwig Prandtl* used in the Lister Tief during the OROMA experiment at 1230 UT 14 August 2002.

[8] The Lister Tief has been selected because one of the most pronounced and dynamic marine sand wavefields in German coastal waters is located in this tidal channel. The R/V *Ludwig Prandtl* was equipped with the following sensors in the period 6–23 September 2004: a parametric sediment echo sounder SES-2000 with a frequency of 12 kHz, a precise differential Global Positioning System (PDGPS), an RD instruments acoustic Doppler current profiler (ADCP) with a frequency of 1200 kHz, a Kelvin Hughes RSR 1000 X band VV polarized river radar with a frequency of 9.42 GHz, a Siggelkow Gerätebau GmbH Soni 3 meteorological sensor system, a ME ecosonde conductivity-temperature-depth (CTD) probe, and handheld cameras. The measurement configuration on board R/V *Ludwig Prandtl* during one of the OROMA experiments on 14 August 2002 is shown in Figure 2.

[9] Current velocity profiles have been measured by the ADCP. Bottom tracking is implemented and an arrangement of 4 downward looking convex transducers was performed in such a way that 2 pairs of transducers pointed in the fore-aft and starboard-port directions, respectively, with an incidence angle of 20°. Almost all surveying profiles of the ADCP measurements across the study area have been obtained on board R/V *Ludwig Prandtl* at a ship speed between 1.5 m s^{-1} and 4.5 m s^{-1}. The ADCP was mounted within the moon pool of the ship at 1.7 m water depth. The current velocity measurements have been recorded continuously from a water depth 2.32 m below the sea surface to 1.2 m above the seabed, separated into water depth cells (bins) of 0.25 m. At the bottom interface the ADCP data have to be considered with caution because of acoustic interference from the bottom. The collected and processed data after each pulse transmission have been averaged over a sampling interval of 5 s. At the end of the sampling interval, a profile of the resulting current velocity relative to the ADCP was generated as a function of range and then stored on the hard disk of the connected computer. The relative accuracy of the current velocity is ±1 cm s^{-1} and the accuracy of the estimated absolute current velocity is ±5 cm s^{-1}.

3. Sea Bottom Topography

[10] Marine sand waves are one of the most conspicuous natural phenomena, especially from a sedimentological point of view. The internal structure, dynamics and morphology of marine sand waves as well as their associated hydrodynamic processes are subjects of several present research activities [*Le Bot and Trentesaux*, 2004].

[11] In this section the behavior of large asymmetrical sand waves (width: 100–350 m) with large lee slopes ($\leq$31°) and associated mega ripples (width: 0.5–2 m) located in the troughs of sand waves will be outlined. A preprocessed map of the sea bottom topography of the whole study area in the Lister Tief as recorded during the OROMA experiment in September 2004 is shown in Figure 3. Sounding tracks at 50 m distances have been gathered by the SES-2000 echo sounder in combination with a PDGPS system. The transducer system of the SES-2000 echo sounder system was installed within the R/V *Ludwig Prandtl* nearly below the PDGPS antenna. The data triplets (x, y, z), with x and y the two horizontal and z the vertical space coordinates, respectively, have been interpolated onto a grid of 7.5 m by 7.5 m and is visualized in a map based on Gauss-Krüger (GK) coordinates in Figure 3. The coverage is 3850 m by 1350 m. A noisy interrupted feature of a large water depth change of a submarine terrain edge ranging from 34 m to 14 m is visible in the northeastern part of the study area. This is due to the applied interpolation technique and will not be considered for further analysis. The location of the side-scan sonar image shown in Figure 4 is marked by *a*, the profile of the analyzed echo sounder data and ADCP measurements presented in Figures 5 and 6 is indicated by AA'.

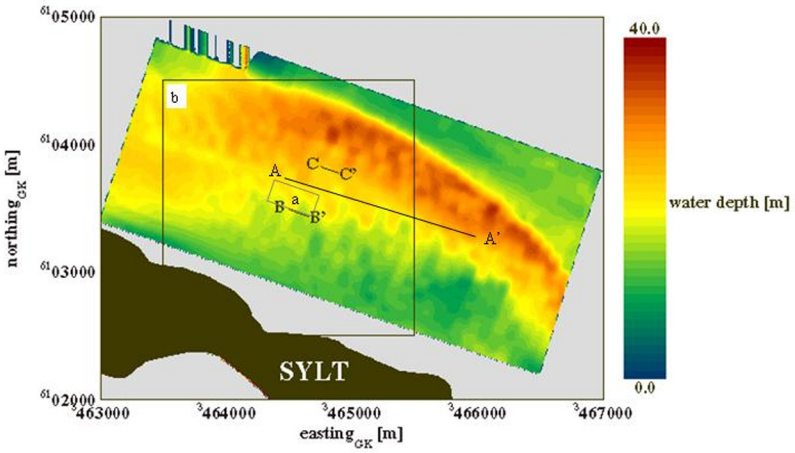

Figure 3. Preprocessed map of the sea bottom topography of the whole study area in the Lister Tief as recorded by the SES-2000 echo sounder in combination with the PDGPS system during the OROMA experiment in September 2004. The data have been interpolated onto a grid of 7.5 m by 7.5 m and are visualized in a map based on Gauss-Krüger (GK) coordinates. The location of the side-scan sonar image shown in Figure 4 is marked by *a*; the profile of the analyzed echo sounder data and ADCP measurements presented in Figures 5 and 6 is indicated by AA'; the location of the NRCS modulation image visualized in Figure 10 is marked by *b*; and the profiles of simulated and measured NRCS modulations due to asymmetric sand waves presented in Figures 11 and 12 are marked by BB' and CC', respectively.

[12] The seabed morphology of the Lister Tief tidal channel is a complex configuration of different bed forms. The marine sand waves investigated in this study are four-dimensional in space and time. Small-scale as well as megaripples are superimposed on sand waves as shown in Figure 4. The sand waves have heights $\leq$11 m and often crest to crest distances (widths) $\geq$300 m. It was shown by *Aliotta and Perillo* [1987] that the orientation of the crestlines and the separation between crests of sand waves varied according to their position in the field. They showed that the two sectors in which the sand wavefield has been divided were almost perfectly separated by bifurcations of the crestlines. The observation of megaripple fans is associated with a large angle of the lee flank and an arcuate orientation of the sand waves [*Aliotta and Perillo*, 1987; *Hennings et al.*, 1993]. Such a megaripple fan located in the trough of an

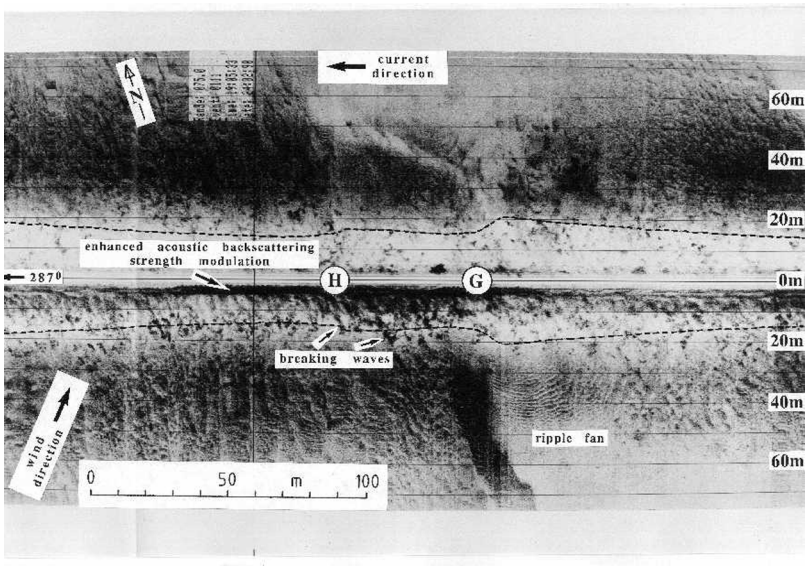

Figure 4. Side-scan record of the 500 kHz sonar system Klein 595 in the sea area of the Lister Tief at 1805 UT 24 February 1990 during ebb tidal phase [from *Hennings et al.*, 1993]. The location is marked by *a* in Figure 3. *G* and *H* indicate the position of sand wave crests. Enhanced acoustic backscatter is shown by dark signatures. Low acoustic backscatter and shadow zones are presented by bright signatures. Dashed lines indicate the water depth profiles below the towed sonar fish. The mean wind and current directions are shown by arrows.

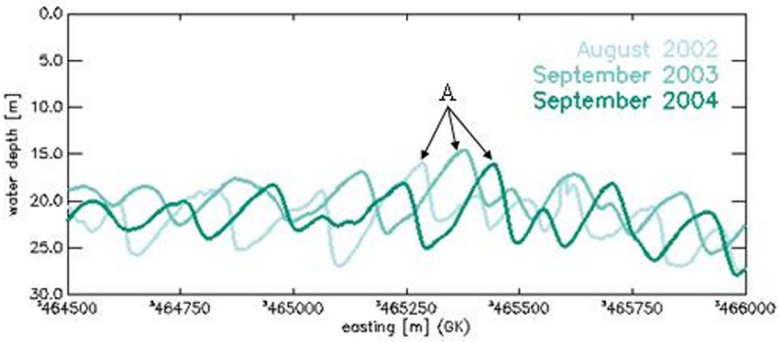

Figure 5. Migration of sand waves in the study area of the Lister Tief. The echo sounding profiles are indicated by the straight line marked as AA' in Figure 3. Three bathymetric surveys have been analyzed during the OROMA experiments in August 2002, September 2003, and September 2004. The asymmetric flood tide–oriented sand wave with a height of 8 m marked by A migrated 80 m per year from west to east.

arcuate sand wave is imaged in Figure 4 showing a side-scan record of the 500 kHz sonar system Klein 595 in the sea area of the Lister Tief (location is indicated by *a* in Figure 3) at 1805 UT 24 February 1990 during ebb tidal phase [*Hennings et al.*, 1993]. Two crests of sand waves are marked by *G* and *H*. The enhanced acoustic backscattering strength modulation (dark signatures) associated with breaking waves was caused by the crests of these two bed forms. The location of the megaripple fan coincided with those stations where both strong horizontal and vertical current shear have been observed [*Hennings et al.*, 1994]. The wind speed was 10 m s^{-1} and the direction was from 220°. Similar sand waves with large slopes of their lee flanks have been also noticed in the Malacca Strait, Southeast Asia [*Keller and Richards*, 1967].

[13] In the past, systematic morphological investigations have been carried out to study the migration of these sand waves [*Ulrich and Pasenau*, 1973]. In the northern section of the test area most of the sand waves have ebb tide–oriented forms; in the southern part most of them are flood tide oriented. In the southeastern part the stoss slopes of sand waves are of the order of $\partial z/\partial x \leq 0.017$ (1°). The lee slopes have maximum values of $\partial z/\partial x = 0.591$ (30.6°). Data analyzed by *Ulrich and Pasenau* [1973] showed that sand waves with a mean height of 3 m migrated about 60 m per year. The migration of sand waves in the study area of the Lister Tief during the OROMA project in August 2002, September 2003, and September 2004 is shown in Figure 5. The profile is indicated by AA' in Figure 3. The asymmetric flood tide–oriented sand wave with a height of 8 m marked by A migrated 80 m per year from west to east due to the local current regime. The islands of Rømø and Sylt are connected by dams to their mainlands and therefore the Lister Tief is the entrance of an artificial tidal bight. During

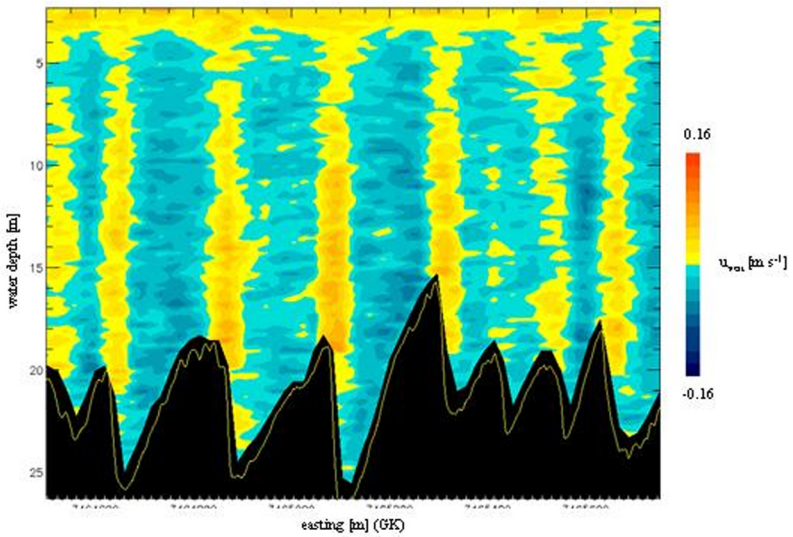

Figure 6. Water depth–dependent vertical component u_{vert} of the current velocity as a function of the horizontal space component perpendicular to the sand wave crest x_{perp}. The ADCP data from the near–water surface to the seabed have been obtained on board R/V *Ludwig Prandtl* during ebb tidal phase at 0500–0515 UT 10 August 2002 along the profile AA' (see Figure 3). Blue shows the downward and yellow shows the upward oriented vertical component u_{vert}.

every tide a water volume of about 5.25×10^8 m^3 passes the tidal channel and is a source of such sand movements.

4. Macroturbulence

[14] Until now the characteristic fluid flow in the water column over marine sand waves is not well understood especially in the vicinity of three dimensional (3-D) marine sand waves. According to *Bennett and Best* [1995] the flow regime can be generally subdivided into five major zones: (1) accelerated, converging flow over the sand wave crest; (2) a zone of flow separation on the crest lee side with its characteristic recirculation pattern; (3) a decelerated wake region overlying the separation cell and extending downstream; (4) an outer, near-surface region overlying this wake; and (5) the downstream growth of a new, internal boundary layer originating at reattachment. Above the separation cell and along the free shear layer associated with this zone, high-turbulence intensities and Reynolds stresses are observed [*Soulsby et al.*, 1991]. The expression "macroturbulence" is used here for sand wave-scale bed forms in contrast to "microturbulence" which is associated with ripple-scale bed forms [*Bennett and Best*, 1995; *Ha and Chough*, 2003]. Recent work of 3-D sand waves by *Maddux et al.* [2003a, 2003b] demonstrated that the nature of the mean flow and turbulence are greatly influenced by the sand wave shape. The crests of sand waves often evolve to sinuous forms because of shearing current speeds u(y). However, the inclination of the underlying seafloor itself has also an additional effect on the magnitude and direction of the tidal current flow.

[15] Experimental and field investigations of sand waves have documented turbulent events called "kolks" and "boils" [*Matthes*, 1947; *Coleman*, 1969]. The so-called "kolk-boil" mechanism is one of predominantly turbulent events occurring over sand waves in fluvial, estuarine, and marine coastal environments [*Ha and Chough*, 2003]. A kolk is a slowly rotating, upward tilting vortex on the stoss face of a subaqueous bed form. A strong kolk may reach the water surface, can create a cloudy columnar sediment-fluid mixture, and forming a raised circular or oval patch at the air-water interface, referred to as a boil [*Matthes*, 1947; *Kostaschuk and Church*, 1993]. These boils are created on a scale that is comparable to the flow depth itself as a first approximation. This mechanism is visualized by so-called "waterspouts," the upward oriented component u_{vert} of the three-dimensional current velocity field measured by the ADCP at the stoss faces of asymmetric marine sand waves in the study area of the Lister Tief [*Hennings et al.*, 2004]. The waterspouts have been measured by the ADCP of the same kind during ebb and flood tidal current phases, respectively. During ebb tidal phase the waterspouts are upwelling events and during flood tidal phase they are associated with downwelling at the steep flanks of these investigated marine sand waves. It has to be noticed here, that observed vertical velocities over two-dimensional (2-D) dunes in a laboratory channel analyzed by *Bennett and Best* [1995] are directed downward above the dune trough and upward over the stoss during flood tidal phase. The waterspouts described here appear to have a different phase relationship to the sand waves. The origin of the kolk at the stoss side of the sand wave is located at the reattachment point. The water depth–dependent vertical component u_{vert} of the current velocity as a function of the horizontal space component perpendicular to the sand wave crest x_{perp} varying between -10 cm s$^{-1} \leq u_{vert} \leq 6$ cm s^{-1} during ebb tidal phase at 0500–0515 UT 10 August 2002 is shown in Figure 6. The downward oriented vertical component (blue) is located at the troughs and gentle slopes of the sand waves. A regular structure of circulation cells of u_{vert} within the water column has been developed during that time of the tidal phase. Marked waterspouts of the direct upward oriented vertical component u_{vert} of the current velocity (yellow) have been developed at the steep flank of sand waves and are superimposed on the divergent zones of the perpendicular component relative to the sand wave crest of the current velocity gradient $\partial u_{perp}/\partial x_{perp}$ [*Hennings et al.*, 2004]. These observations are consistent with the theory of the radar imaging mechanism of sea bottom topography presented by *Alpers and Hennings* [1984].

[16] Boils manifested at the sea surface observed near arcuate crests of flood tide–oriented sand waves (see Figure 4) in the sea area of the Lister Tief are shown in Figure 7. The handheld camera image was acquired from on board the R/V *Ludwig Prandtl* at 1519 UT 15 August 2002 during flood tidal current phase and a wind speed of 2–3 m s^{-1}. Similar observations of boils have been made also in the Brahmaputra river [*Coleman*, 1969]. Associated with the generation of kolks is the formation of megaripple fans at the trough of marine sand waves due to flow separation (see section 3). *Maddux et al.* [2003a] showed that the fluid was steered near the seabed around the highs and lows of their investigated 3-D sand waves. The most rapid flows have been observed at the sand wave crest, halfway between the maxima and minima of the crest line. It has been shown by *Nimmo Smith et al.* [1999] that boils can even be generated by the tidal stream of a flat seabed without sand waves or other notable bed forms. These boils were visible in upward pointing side-scan sonar images because the downwelling at their upwind boundary results in the local accumulation of bubbles and wave steepening of short surface gravity waves or even breaking with bubble production which enhancing the acoustic scattering there. Because of these observations it is supposed here that such hydrodynamic modulation processes can influence the radar imaging mechanism of particular sand waves as well. At the moment little is known of how boils as surface manifestations of slowly rotating, upward directed vortices approach and interact with the current at the sea surface. If boils indeed play a role of the NRCS modulation associated with 3-D sand waves at low wind speeds ≤ 5 m s^{-1} will be investigated by using the German remote sensing satellite TerraSAR-X with its high spatial resolution of up to 1 m. For the first time, it is expected, that turbulence patterns or boils can be detected from space relative to the orientation of sand wave crests at the sea surface. The manifestation of boils relative to the radar signatures of sand waves will be analyzed in dependence on tidal current speed and direction as well as wind speed and direction, respectively, during flood and ebb tidal current phases. The schematic sketch of sand wave-related macroturbulence caused by ebb tidal currents over flood tide–oriented sand waves, the associated secondary circulation regimes described above, as well as coordinate

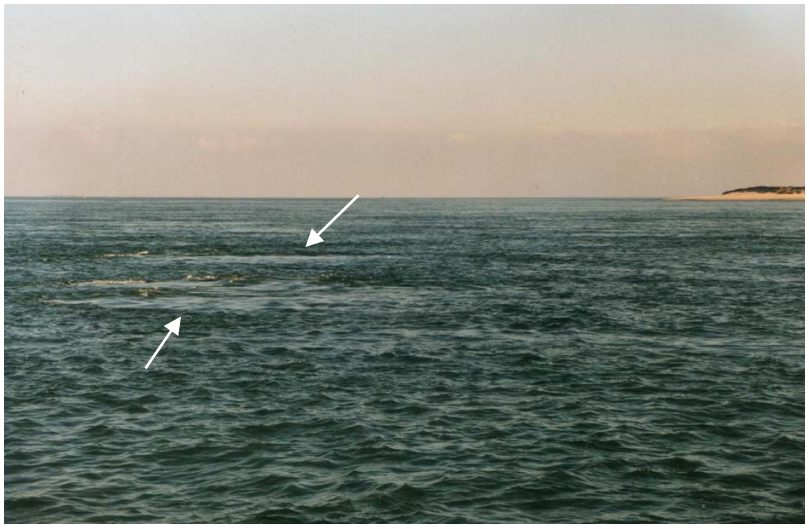

Figure 7. Handheld camera picture of turbulence patterns (marked by arrows) in the sea area of the Lister Tief acquired from on board the R/V *Ludwig Prandtl* at 1519 UT 15 August 2002 during flood tidal current phase.

systems and definition of symbols used in section 6 are visualized in Figure 8.

5. Shipborne Radar Data

[17] The shipborne coastal monitoring radar of the GKSS Research Center is based on a Kelvin Hughes RSR 1000 X band (9.42 GHz) VV polarized river radar and was mounted on board the R/V *Ludwig Prandtl* during the OROMA experiments. The important progress realized within the OROMA project is the availability of calibrated shipborne X band radar data.

[18] The backscattering cross section σ of a point target is defined by [e.g., *Tomiyasu*, 1978; *Hovanessian*, 1980]

$$\sigma = \frac{P_R^{dB}(4\pi)^3 R^4 L_{SL}}{P_S^W G^2 \lambda_{radar}^2} \quad (1)$$

where R is the distance between the radar antenna and the scattering target, P_S^W is the transmitted power, P_R^{dB} is the received power, G is the theoretical gain of the antenna, and L_{SL} is the total system loss. The dimension of σ is defined by a plane. For plane targets like the sea surface the backscattering cross section is expressed by square meters per plane unit and defined as normalized radar cross section (NRCS). In the following the symbol σ will be used for the local NRCS in contrast to σ_0 as the averaged background NRCS.

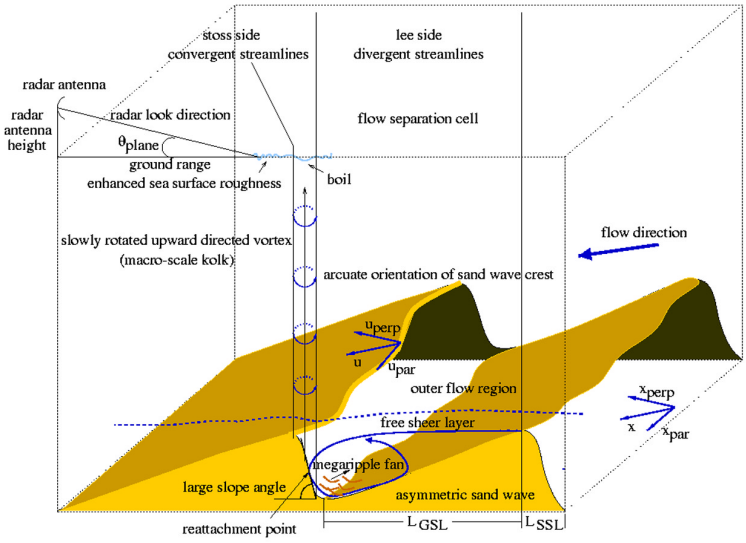

Figure 8. Schematic sketch of the characteristic fluid flow in the water column, the macroturbulence mechanism caused by ebb tidal currents over flood tide–oriented marine sand waves, as well as coordinate systems and definition of symbols used in section 6.

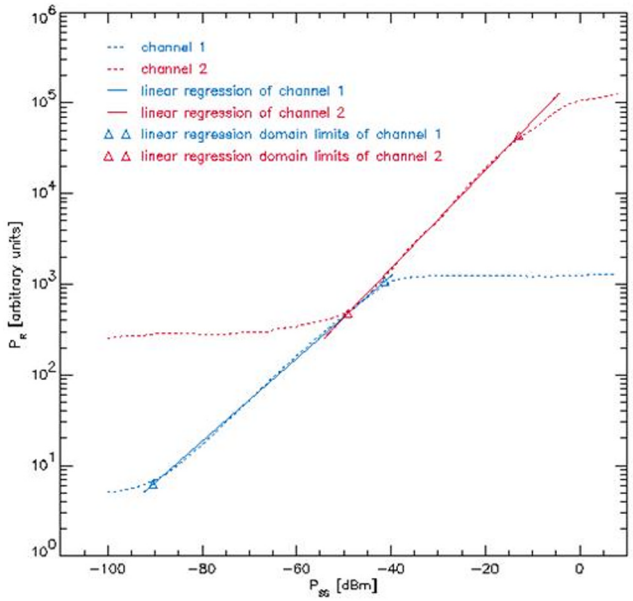

Figure 9. Calibration curves used for the shipborne Kelvin Hughes RSR 1000 X band (9.42 GHz) VV polarized river radar during the Lister Tief experiment in September 2004.

[19] The following values have been used for the calibration method according to (1): P_S^W = 4900 W, G = 25 dB, L_{SL} = 3 dB, and λ_{radar} = 0.032 m. A well defined signal power of 9.42 GHz produced by a high-frequency (HF) generator has been sent to the entrance of the waveguide at the radar antenna and was stored via a personal computer using the radar recording system software. The analog digital converter made use of two channels: channel 1 with large amplification and channel 2 with low amplification, respectively. By varying the signal power of the HF generator between −100 dBm and 8 dBm in steps of 2 dBm and averaging the received power for each dBm value the amplitude characteristics of the two channels have been achieved. The dBm notation represents a power level in decibels relative to 1 mW. Therefore the relations defined by 1 mW = 0 dBm = 223.6 mV at a resistance value of 50 Ω have been used. Then the linear correlation domain was determined for each channel separately. Within this linear correlation domain the measured backscattered radar signals from the sea surface have been converted to corresponding P_R^{dB} values. The backscattered values outside of the linear correlation domain have been set to the extrema values at both sides of this domain. The result of the calibration is shown in Figure 9 where P_R (in arbitrary units) is a function of the signal power produced by the HF generator. The transition point shown in Figure 9 is defined as the intersection of the linear correlation domain curves characterized by channel 1 and channel 2. Because of this calibration characteristic of the received power the corresponding values of P_R^{dB} have been calculated from the backscattered radar signals of the sea surface and are inserted in (1) obtaining calibrated local NRCS data.

[20] The NRCS modulation caused by marine sand waves via the associated surface current variation has been defined as

$$\frac{\delta\sigma}{\sigma_0} = \frac{\sigma}{\sigma_0} - 1 \tag{2}$$

where σ_0 is the averaged background NRCS of the considered area. NRCS modulation data have been measured and mapped during ebb and flood tidal current phases, respectively. The backscattered radar signals from the water surface have been received by a fixed antenna (not a rotating one) using the so-called radar scanning mode. This kind of mode is comparable with the acoustic side-scan imaging mode used by sonar and multibeam echo sounders. The profiles have been arranged in such a way that the R/V *Ludwig Prandtl* followed the orientations of the sand wave crests. The look direction of the radar antenna was perpendicular to the profiles expecting the most useful NRCS modulation signatures caused by marine sand waves. The distance of the profiles was 100 m. Radar data from a ground range of 562 m beginning at a distance of 112.5 m from the foot point of the antenna at the sea surface perpendicular to the ship track have been further processed. As an example Figure 10 shows a composite of 23 single radar images taken at 0800–1325 UT 7 September 2004 in the sea area of the Lister Tief during ebb tidal current phase. The location of the NRCS modulation image visualized in Figure 10 is marked by *b* and the profiles of simulated and measured NRCS modulations due to asymmetric sand waves presented in Figures 11 and 12 are marked by BB' and CC', respectively, in Figure 3. At the acquisition time interval of the radar composite wind speeds between 4.0 m s^{-1} and 7.5 m s^{-1} from easterly directions have been measured. The NRCS modulation shown in Figure 10 is dominated by bright signatures of asymmetric ebb as well as flood tide–oriented marine sand waves. Enhanced roughness patterns are located within the convergent zones of the tidal current gradient above the slopes of sand waves as indicated in Figure 8. The NRCS modulations show also a variation along the signatures itself. This is indeed reflected by the 3-D marine sand waves shown in Figure 3. The peak in the southern part of the study area is the radar signature of buoy 13.

6. Theory

[21] For most ocean wave conditions and radar incidence angles greater than 15°, the quasi-specular point scattering contribution to the mean radar image intensity is small compared with the Bragg-scattering contribution. Under some special conditions there are indications that it may also contribute at larger incidence angles than 15°. It is well known that the magnitudes of water surface slopes, the directional character of the sea surface roughness and the level of microwave scattering are related in complicated ways to wind, fetch, current gradients, atmosphere stability, and other meteorological and oceanographic parameters. The nature of these dependencies and interactions are active and controversial areas of research. Specular reflection occurs when radiation is scattered into a given direction from surface regions with slopes such that the local specular

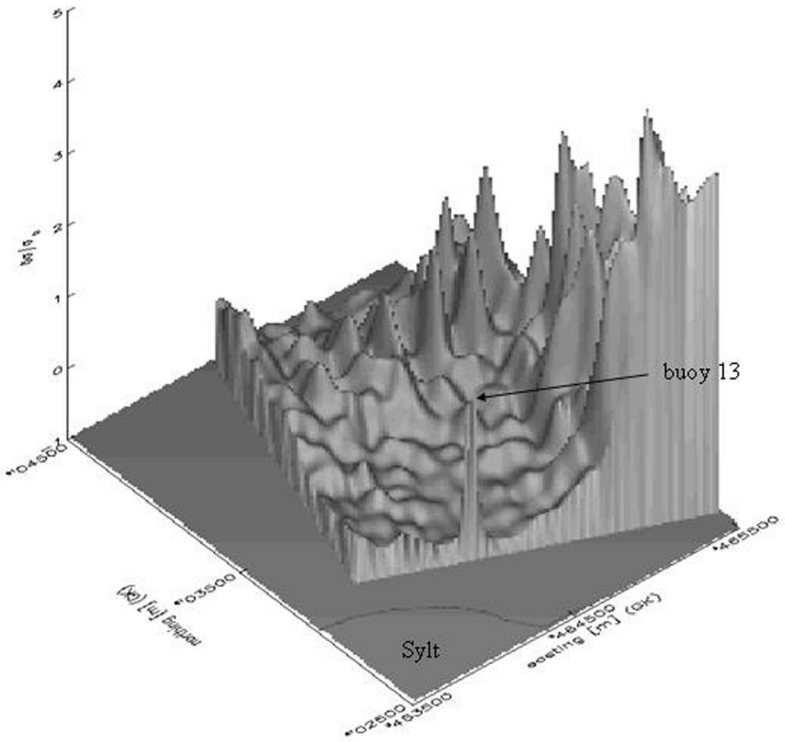

Figure 10. NRCS modulation composite of 23 single radar images taken at 0800–1325 UT 7 September 2004 from on board the R/V *Ludwig Prandtl* in the sea area of the Lister Tief during ebb tidal current phase. The location of the NRCS modulation composite is marked as a frame indicated by *b* in Figure 3. The NRCS modulation imaged as bright signatures is caused by asymmetric ebb and flood tide–oriented marine sand waves. The peak in the southern part of the study area is the radar signature of buoy 13.

direction coincides with the scattering direction. The quasi-specular scattering theory can be applied if the wavelengths of waves in the ocean contributing to the mean square surface slope are greater than the wavelength of the microwave. In general, the mean squared slope of such waves is small. However, this is considerably different if waves are influenced by a surface current gradient. Very steep disturbed slopes of the order of 10° or more can arise in the converging zone of the current correlated with the slope regions of marine sand waves. Especially trochoidal shapes of water waves can be generated by such a kind of wave-current interaction at low to moderate wind speeds. These trochoidal shaping waves are producing an ensemble average of facets which create quasi-perpendicular planes relative to the transmitted radar beam. This could be an indication that short water waves contribute more as specular scattering targets to the imaging mechanism than predicted from the probability density function of slopes of the rough ocean surface without existing wave-current interaction. There exist also steep small gravity waves in this zone which tend to become sharp wedges just before they break and breaking waves themselves. In this paper we investigate if the quasi-specular scattering theory in combination with the weak hydrodynamic interaction theory can be applied where extremely steep slopes acting as backscattered mirrors.

[22] The normalized radar backscattering cross section (NRCS) σ_0 for an isotropic rough ocean surface obeying Gaussian statistics according to the incident angle dependency for quasi-specular scattering is given by *Valenzuela* [1978]

$$\sigma_0(\theta_0) = \frac{|R(0)|^2}{s_0^2} \frac{1}{\cos^4 \theta_0} \exp\left(-\frac{\tan^2 \theta_0}{s_0^2}\right) \tag{3}$$

where R(0) is the Fresnel reflection coefficient for normal incidence, θ_0 is the angle of incidence, and s_0^2 is the total variance of slopes created by ocean waves.

[23] For the total variance of slopes the mean square slope of water waves derived by *Cox and Munk* [1954] empirically is used:

$$s_0^2 = 0.003 + 0.00512 U_w \pm 0.004 \tag{4}$$

where U_w is the wind speed.

[24] Rewriting the total variance of slopes and the incidence angle as sums of a constant equilibrium term and a time-dependent perturbation term, respectively, yields

$$s^2 = s_0^2 + \delta s^2 \tag{5}$$

and

$$\theta = \theta_0 + \delta\theta \tag{6}$$

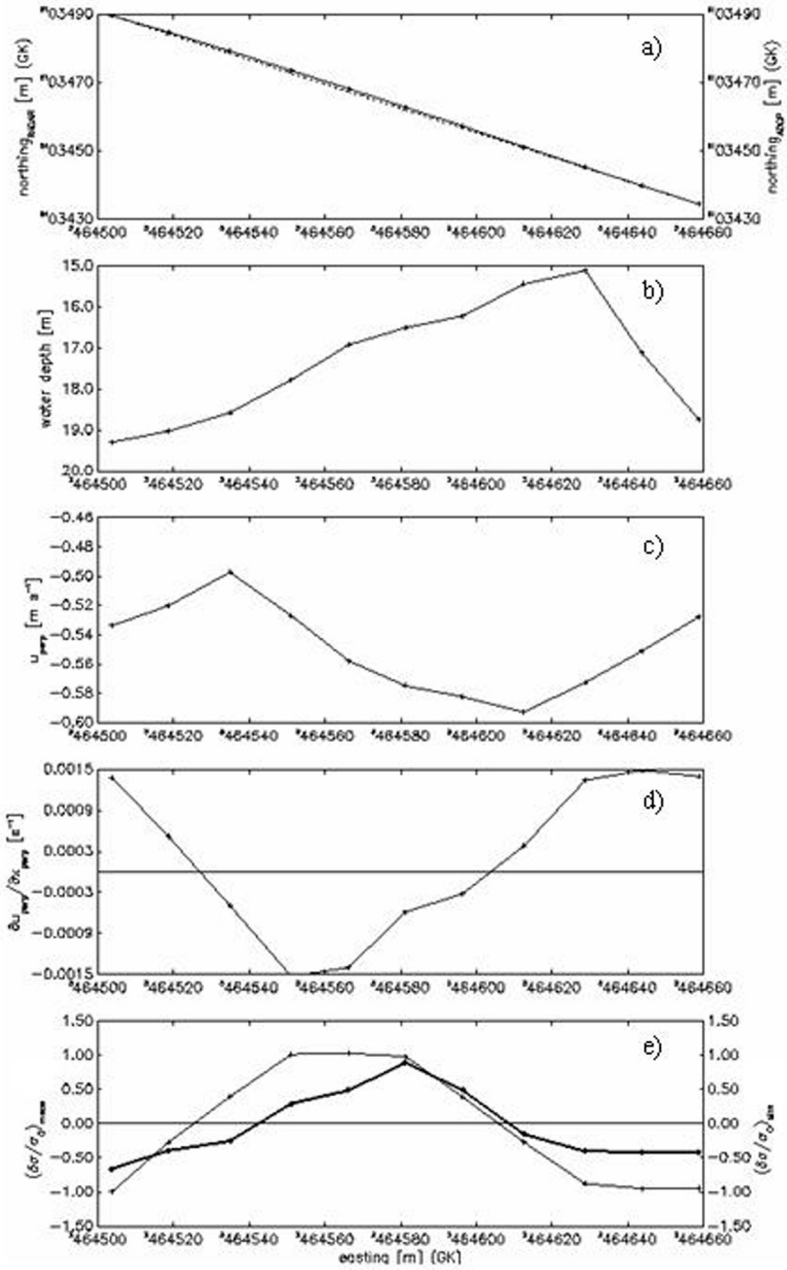

Figure 11. Analyzed echo sounder and ADCP data taken at 1001–1002 UT 6 September 2004 and measured radar data taken at 0826–0836 UT 7 September 2004 during ebb tidal phase for the flood tide–oriented marine sand wave: (a) positions of the analyzed water depth and ADCP profile ($\text{northing}_{\text{ADCP}}$, solid line, marked by BB' in Figure 3) as well as measured NRCS modulation profile ($\text{northing}_{\text{RADAR}}$, dashed line) based on Gauss-Krüger (GK) coordinates, (b) water depth as a function of position, (c) mean vertical integrated current speed u_{perp} perpendicular to the sand wave crest as a function of position, (d) strain rate or gradient of the perpendicular component relative to the sand wave crest of the current velocity $\partial u_{\text{perp}}/\partial x_{\text{perp}}$ as a function of position, and (e) simulated NRCS modulation $(\delta\sigma/\sigma_0)_{\text{sim}}$ applying (10) (thin solid line) and measured NRCS modulation $(\delta\sigma/\sigma_0)_{\text{meas}}$ (thick solid line) as a function of position.

In the following the effective incidence angle θ_0 is used for a real sea surface with roughness which no longer coincides with the incidence angle for a plane sea surface. The effective incidence angle θ_0 is given by

$$\theta_0 = \theta_{\text{plane}} + \theta_{\text{rough}} \tag{7}$$

where θ_{plane} is the incidence angle for a plane surface. The incidence direction of radar transmission is placed in a plane which is defined perpendicular to the air-water boundary plane and hence includes also the normal relative to this boundary plane. The incidence angle is thereupon defined between this normal and the incident ray transmitted from

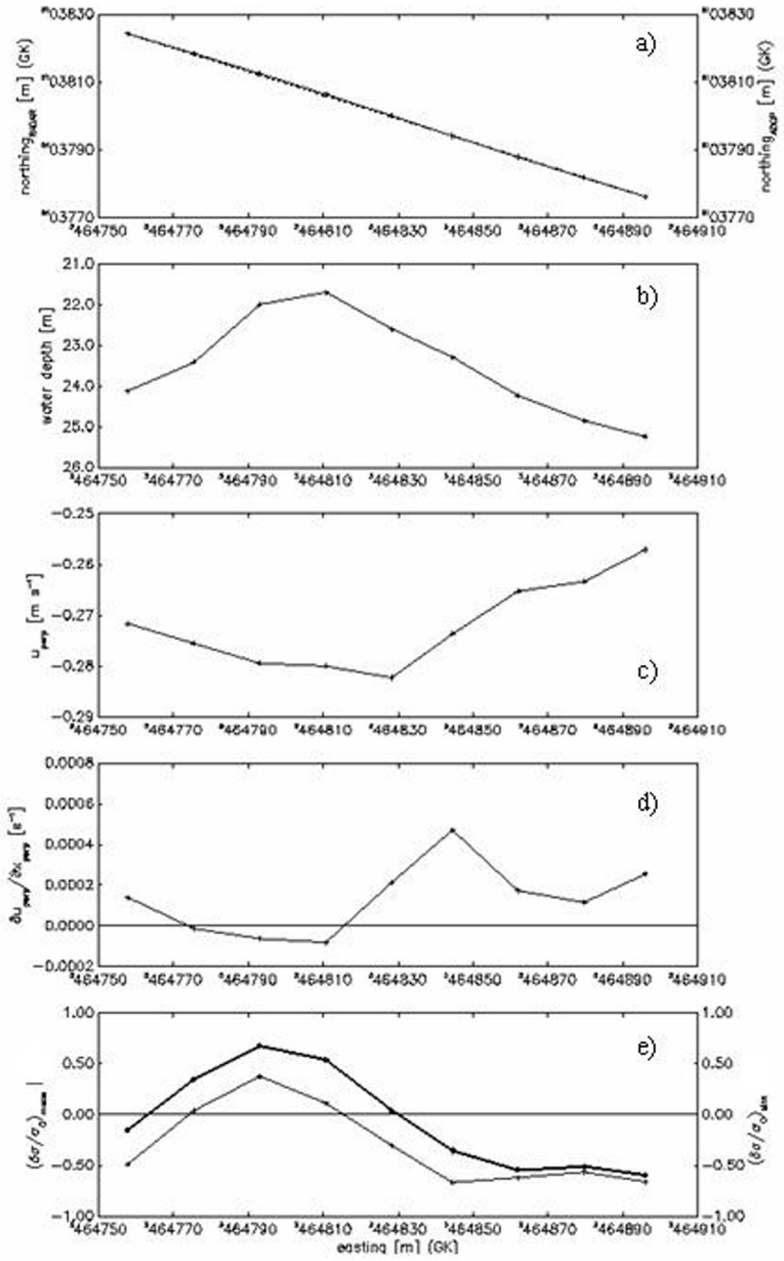

Figure 12. Analyzed echo sounder and ADCP data taken at 1203–1204 UT 6 September 2004 and measured radar data taken at 0826–0836 UT 7 September 2004 during ebb tidal phase for the ebb tide–oriented marine sand wave: (a) positions of the analyzed water depth and ADCP profile ($northing_{ADCP}$, solid line, marked by CC' in Figure 3) as well as the measured NRCS modulation profile ($northing_{RADAR}$, dashed line) based on Gauss-Krüger (GK) coordinates, (b) water depth as a function of position, (c) mean vertical integrated current speed u_{perp} perpendicular to the sand wave crest as a function of position, (d) strain rate or gradient of the perpendicular component relative to the sand wave crest of the current velocity $\partial u_{perp}/\partial x_{perp}$ as a function of position, (e) simulated NRCS modulation $(\delta\sigma/\sigma_0)_{sim}$ applying (10) (thin solid line), and measured NRCS modulation $(\delta\sigma/\sigma_0)_{meas}$ (thick solid line) as a function of position.

the radar antenna. Here the incidence angle θ_{plane} is identical with the complementary angle called grazing angle (see Figure 8).

[25] The square tangent of the incidence angle of the background rough sea surface as a function of U_w (see (4)) is derived by

$$\tan^2\theta_{rough} = s_0^2 \tag{8}$$

As a first approximation assuming that the time-dependent perturbation terms in (5)–(6) caused by the disturbance of the surface current $\delta U(\mathbf{x})$ due to marine sand waves obey also Gaussian distributions, then the disturbed NRCS $\delta\sigma$ is

given by

$$\delta\sigma = \sigma - \sigma_0 = \frac{|R(0)|^2}{\left(s_0^2 + \delta s^2\right)} \frac{1}{\cos^4(\theta_0 + \delta\theta)} \exp\left(-\frac{\tan^2(\theta_0 + \delta\theta)}{s_0^2 + \delta s^2}\right) - \sigma_0 \quad (9)$$

where σ is the local NRCS as defined by (1). The NRCS modulation $\delta\sigma/\sigma_0$ due to quasi-specular scattering is defined by

$$\frac{\delta\sigma}{\sigma_0} = \frac{\sigma}{\sigma_0} - 1 = \frac{s_0^2 \cos^4\theta_0}{\left(s_0^2 + \delta s^2\right)\cos^4(\theta_0 + \delta\theta)} \frac{\exp\left(\frac{\tan^2\theta_0}{s_0^2}\right)}{\exp\left(\frac{\tan^2(\theta_0 + \delta\theta)}{s_0^2 + \delta s^2}\right)} - 1 \quad (10)$$

with the square tangent of the disturbed incidence angle

$$\tan^2\delta\theta = +\delta s^2, \ \frac{\partial u_{perp}}{\partial x_{perp}} \le 0 \quad (11a)$$

$$-\tan^2\delta\theta = -\delta s^2, \ \frac{\partial u_{perp}}{\partial x_{perp}} > 0 \quad (11b)$$

and the disturbed square slope

$$\delta s^2 = \int_{k_0}^{k_c} \mathbf{k}^2(\mathbf{x})\delta F(\mathbf{x}, \mathbf{k})d\mathbf{k} \quad (12)$$

where x_{perp} is the space variable defined perpendicular to the sand wave crest (see Figure 8), $\mathbf{k}$ is the wave number vector of short gravity waves, k_0 is the lower limit of the wave number producing quasi-specular scattering modulation, k_c is the maximum wave number where the effect of surface tension is negligible, $\partial u_{perp}/\partial x_{perp}$ is the gradient or strain rate of the current velocity perpendicular to the sand wave crest (see Figure 8), and $\delta F(\mathbf{x}, \mathbf{k})$ is the perturbation term of the wave energy density spectrum in the short gravity wave regime caused by wave-current interaction applying weak hydrodynamic interaction theory [*Alpers and Hasselmann*, 1978]. The perturbation term $\delta F(\mathbf{x}, \mathbf{k})$ can be interpreted as the density of contributions to δs^2 per unit area of $\mathbf{k}$ space. The spatial scale of the waves responsible for the quasi-specular scattering modulation was assumed to be in the range of wavelengths $\lambda_c = 2\pi/k_c = 0.032$ m and $\lambda_0 = 2\pi/k_0 = 7.5$ m. These values have been selected because the microwave wavelength of the radar is $\lambda_{radar} = 0.032$ m and the spatial resolution of the radar is $\rho_{radar} = 7.5$ m. The parameters $\delta\theta$ and δs^2 expressed by (11)–(12) are defined positive as well as negative depending on the sign of the current gradient or strain rate $\partial u_{perp}/\partial x_{perp}$. Short surface waves are stretched within a divergent current regime and the square tangent of the local incidence angle and the total variance of local slopes are reduced from equilibrium because of a diminished wave height spectrum $\psi(\mathbf{k})$ or wave energy density spectrum $F(\mathbf{k})$. On the other hand short surface waves are compressed within a convergent current regime where the square tangent of the local incidence angle and the total variance of local slopes are enhanced from equilibrium due to an increased wave height spectrum $\psi(\mathbf{k})$ or wave energy density spectrum $F(\mathbf{k})$. To derive (12) the relationship shown by *Phillips* [1977] has been used where the mean square slope of sea surface waves can be obtained from the wave height spectrum $\psi(\mathbf{k})$ or wave energy density spectrum $F(\mathbf{k})$ of ocean gravity waves

$$s^2 = \int k^2 F(\mathbf{k})d\mathbf{k} \quad (13)$$

The integration should cover the possible range of the wave number. Considering (13) statistically this relation is also the common definition of the variance of a continuously distribution function. The relationship between $\psi(\mathbf{k})$, $F(\mathbf{k})$ and the wave action density spectrum $N(\mathbf{k}) = F(\mathbf{k})\,(\omega'(k))^{-1}$ is defined by [*Holliday et al.*, 1986]

$$F(\mathbf{k}) = \omega'(k)N(\mathbf{k}) = \frac{\omega'(k)^2}{k}\psi(\mathbf{k}) \quad (14)$$

with the wave height spectrum

$$\psi(k) = a_P k^{-4} \quad (15)$$

where a_P is known as the Phillips constant. Because of measurements by *Stolte* [1990], the empirical relation for a_P as a function of wind speed $U_w \le 8$ m s^{-1} is used:

$$\log_{10} a_p = -2.90 + 3.06 \cdot 10^{-1} U_w - 1.85 \cdot 10^{-2} U_w^2 \quad (16)$$

The dispersion relation for gravity waves in (14) is defined by

$$\omega' = (gk)^{1/2} \quad (17)$$

For the modulation of the first-order perturbed wave energy density spectrum $\delta F/F_0 = (F - F_0)/F_0$ (with F_0 as the unperturbed wave energy density spectrum) the expression derived by *Alpers and Hennings* [1984] is used:

$$\frac{\delta F}{F_0} = -4.5 \frac{\partial u_{perp}}{\partial x_{perp}} \left((\mathbf{c}_g + \mathbf{u}_0)\frac{1}{L} + \mu\right)^{-1} \quad (18)$$

with the absolute value of the group velocity for gravity waves

$$|\mathbf{c}_g| = \frac{1}{2}\frac{\omega'}{k} \quad (19)$$

where $\mathbf{u}_0$ is the mean current velocity of the undisturbed sea area, μ is the relaxation rate parameter, g is the acceleration of gravity, and L denotes the length scale of the slope of the bed form. The length scale of the slope L is different for asymmetric sand waves as shown in Figure 8; $L = L_{SSL}$ is the length scale of the steep slope and $L = L_{GSL}$ is the length scale of the gentle slope of the sand wave, respectively.

[26] The result of (18) is derived by using the action balance or radiation balance equation based on weak hydrodynamic interaction theory according to *Alpers and Hasselmann* [1978]. In this kind of transport equation the variation of the spectral energy density of short waves in a slowly varying current field is described. This implies that a slowly varying surface current is be able creating only small magnitudes of the disturbed square slope. These conditions are often not fulfilled within a strong current gradient caused by large slopes of marine sand waves. On the other hand according to the weak hydrodynamic interaction theory it is sufficient that the strain rate has to be much less than the radian frequency of short surface water waves. This condition has been fulfilled during the OROMA experiments (see section 7).

7. Simulated and Measured NRCS Modulation

[27] During the OROMA experiments it was not possible to take all measurements from on board the R/V *Ludwig Prandtl* parallel and normal to the sand wave crests quasi-simultaneously. However, both types of information are needed according to the theory presented in section 6. The water depth and current velocity data gathered at 1001–1002 UT 6 September 2004 and at 1203–1204 UT 6 September 2004, respectively, are oriented normal to the sand wave crests. The radar profiles of measured NRCS data have been taken at 0826–0836 UT 7 September 2004 and are oriented parallel to the sand wave crests. All data sets have been acquired during ebb tidal current phase and under comparable wind speed and wind direction conditions. Therefore both data sets have been merged. Results are presented for a flood tide as well as for an ebb tide–oriented marine sand wave in Figures 11 and 12, respectively. The positions of the first analyzed water depth profile which is identical with the ADCP profile marked by BB' in Figure 3 as well as the measured NRCS modulation profile based on GK coordinates are shown in Figure 11a. The water depth as a function of position is presented in Figure 11b. This flood tide–oriented sand wave has a width of 155.1 m and a height of 4.19 m. The mean vertical integrated current speed u_{perp} perpendicular to the sand wave crest is presented in Figure 11c. A maximum current speed of $u_{perp}^{max} = 0.59$ m s^{-1} has been measured at the crest of the sand wave. The variation of the current speed between the trough and crest of the sand wave is $\Delta u_{perp} = 0.09$ m s^{-1}. Figure 11d shows the strain rate or the gradient of the perpendicular component relative to the sand wave crest of the current velocity $\partial u_{perp}/\partial x_{perp}$ using the measured ADCP data presented in Figure 11c. These data show the typical distribution of divergent and convergent flow patterns associated with asymmetrical sand waves and confirms the theory developed by *Alpers and Hennings* [1984]. Minimum and maximum values of the strain rate of -0.0015 s^{-1} and 0.0015 s^{-1} have been calculated. The comparison of simulated NRCS modulation $(\delta\sigma/\sigma_0)_{sim}$ with measured NRCS modulation $(\delta\sigma/\sigma_0)_{meas}$ as a function of position is shown in Figure 11e. The calculations for $(\delta\sigma/\sigma_0)_{sim}$ using (10) are carried out for $k_0 = 2\pi/\lambda_0 = 0.84\ m^{-1} \le k \le k_c = 2\pi/\lambda_{radar} = 196.35\ m^{-1}$, $g = 9.81$ m s^{-2}, $|\mathbf{u}_0| = 0.40$ m s^{-1}, $L_{SSL} = 30$ m, $L_{GSL} = 125.1$ m, $\mu = 0.059$ s^{-1}, $U_w = 4.5$ m s^{-1} with an easterly wind direction coming from 92.10°, and $\theta_{plane} = 1.3°$. The value for μ has been obtained by measurements derived by *Hennings et al.* [2001] as the interpolated average value at $U_w = 4.5$ m s^{-1}. For the current gradient $\partial u_{perp}/\partial x_{perp}$ the data based on ADCP measurements shown in Figure 11d have been used for $(\delta\sigma/\sigma_0)_{sim}$. The simulated NRCS modulation $(\delta\sigma/\sigma_0)_{sim}$ presented in Figure 11e shows a maximum modulation $(\delta\sigma/\sigma_0)_{sim}^{max} = 1.05$ at the gentle slope of the sand wave. The measured maximum NRCS modulation $(\delta\sigma/\sigma_0)_{meas}^{max} = 0.84$ is located also at the gentle slope of the sand wave but with a distinct offset of 15 m in upstream direction of the tidal current. The value of the measured minimum modulation $(\delta\sigma/\sigma_0)_{meas}^{min} = -0.50$ in the divergent region at the steep slope of the sand wave is lower than the value of the simulated modulation $(\delta\sigma/\sigma_0)_{sim}^{min} = -0.93$.

[28] The positions of the second analyzed water depth profile which is identical with the ADCP profile marked by CC' in Figure 3 as well as the measured NRCS modulation profile based on GK coordinates are shown in Figure 12a. Water depth as a function of position is shown in Figure 12b. This ebb tide–oriented sand wave has a width of 138.2 m and a height of 3.55 m. The mean vertical integrated current speed u_{perp} perpendicular to the sand wave crest is presented in Figure 12c. A maximum current speed $u_{perp}^{max} = 0.28$ m s^{-1} has been measured at the crest of the sand wave. The variation of the current speed between the trough and crest of the sand wave is $\Delta u_{perp} = 0.02$ m s^{-1}. The strain rate or gradient of the perpendicular component relative to the sand wave crest of the current velocity $\partial u_{perp}/\partial x_{perp}$ is shown in Figure 12d. Minimum and maximum values of the strain rate of -0.0001 s^{-1} and 0.0005 s^{-1} have been calculated. The comparison of simulated NRCS modulation $(\delta\sigma/\sigma_0)_{sim}$ with measured NRCS modulation $(\delta\sigma/\sigma_0)_{meas}$ as a function of position is shown in Figure 12e. The calculations for $(\delta\sigma/\sigma_0)_{sim}$ applying (10) are carried out for $k_0 = 2\pi/\lambda_0 = 0.84\ m^{-1} \le k \le k_c = 2\pi/\lambda_{radar} = 196.35\ m^{-1}$, $g = 9.81$ m s^{-2}, $|\mathbf{u}_0| = 0.27$ m s^{-1}, $L_{SSL} = 52.9$ m, $L_{GSL} = 85.3$ m, $\mu = 0.058$ s^{-1} (according to *Hennings et al.* [2001]), $U_w = 3.9$ m s^{-1} with an easterly wind direction of 118.24°, and $\theta_{plane} = 2.6°$. For the current gradient $\partial u_{perp}/\partial x_{perp}$ the data based on ADCP measurements shown in Figure 12d have been used for the simulation of $(\delta\sigma/\sigma_0)_{sim}$. The simulated NRCS modulation $(\delta\sigma/\sigma_0)_{sim}$ shows a maximum modulation $(\delta\sigma/\sigma_0)_{sim}^{max} = 0.39$ at the steep slope of the sand wave and also the measured maximum NRCS modulation $(\delta\sigma/\sigma_0)_{meas}^{max} = 0.66$ is located at the same position. However, the value of the measured minimum modulation $(\delta\sigma/\sigma_0)_{meas}^{min} = -0.60$ at the easterly divergent region associated with the gentle slope of the sand wave is somewhat lower than the simulated one $(\delta\sigma/\sigma_0)_{sim}^{min} = -0.70$.

8. Discussion and Conclusions

[29] Radar signatures of sea bottom topography are dominated by Bragg scattering theory since most of the imaging radars operate at incidence angles between 20° and 70° [*Valenzuela*, 1978]. A radar scattering theory of NRCS modulation caused by submarine bed forms at very low grazing angle illumination generally accepted by the scientific community still not exists until now. However, new remote sensing monitoring technologies such as shoreborne and shipborne imaging radars applied for coastal monitoring

purposes become more and more important. This subject was the main motivation to investigate if the quasi-specular scattering theory can be applied at very low grazing angle to explain the X band radar imaging mechanism of marine sand waves. The theoretical model presented here is not capable of explaining all aspects of the NRCS modulation due to marine sand waves quantitatively. Nevertheless, it is proposed that the quasi-specular scattering theory at very low grazing angle is a viable first-order theory because the results of the simulated NRCS modulation show the qualitative trend, but do not always quantitatively match the measured NRCS modulation profiles. According to Bragg scattering theory, the NRCS for small water surface waves is proportional to the wave height spectral density $\psi(\mathbf{k})$ at the Bragg backscatter wave numbers. For quasi-specular scattering theory from a rough ocean surface, the NRCS is proportional to the total variance of slopes created by ocean surface waves. The relaxation rate μ is one of the most crucial parameters in weak hydrodynamic interaction theory and has to be taken into consideration applying the presented theory. Comprehensive discussions concerning μ have been published by *Caponi et al.* [1988] and *Hennings et al.* [2001]. Another crucial point was the scarce availability of calibrated NRCS data based on nautical ship radars. Within the OROMA project calibrated shipborne X band radar data have been made available and have been compared with simulated NRCS modulation data. The first comparisons of simulated and measured NRCS modulations show encouraging results, but should be treated with some caution because NRCS and current velocity could not be measured simultaneously within the experimental setup. Simultaneously measured ADCP and NRCS data are needed, because the current gradient or strain rate is one of the most important parameters of the applied weak hydrodynamic interaction theory. A new measurement configuration concerning this aspect has to be reflected on for future experiments.

[30] From the results derived in this paper the following conclusions can be drawn for the X band radar imaging mechanism at very low grazing angle of flood and ebb tide–oriented sand waves during ebb tidal current phase for wind speeds ≤ 8 m s^{-1} and water depths <50 m:

[31] 1. The existence of a significant upward oriented vertical component u_{vert} of the three-dimensional current velocity field measured by the ADCP has been recorded. Marked waterspouts of u_{vert} have been measured in a more or less straight line in the vicinity of crests above steep slopes of flood tide–oriented marine sand waves. These waterspouts created by u_{vert} produce upwelled water and create turbulence patterns at the water surface. The upward oriented patterns of u_{vert} are simultaneously superimposed on the divergent zones of $\partial u_{perp}/\partial x_{perp}$. The downward oriented vertical component of u_{vert} is located at the troughs and gentle slopes of the marine sand waves. A regular structure of circulation cells of u_{vert} within the water column has been initiated at 0500–0515 UT 10 August 2002 during ebb tidal current phase. This implies that mass is not only be conserved by an acceleration or deceleration of the flow in relation to marine sand waves. Upwelling and downwelling of the three dimensional current field also contribute significantly to the extensive circulation mechanism above marine sand waves in the study area of the Lister Tief.

[32] 2. The water depth profiles of flood tide–oriented sand waves show a maximum sand wave migration rate of 80 m per year from west to east between August 2002 and September 2004.

[33] 3. The simulated NRCS modulation $(\delta\sigma/\sigma_0)_{sim}$ and the measured NRCS modulation $(\delta\sigma/\sigma_0)_{meas}$ have the same order of magnitude; the difference between $(\delta\sigma/\sigma_0)^{max}_{sim}$ and $(\delta\sigma/\sigma_0)^{max}_{meas}$ of the ebb tide–oriented sand wave is 27% and the difference between $(\delta\sigma/\sigma_0)^{max}_{sim}$ and $(\delta\sigma/\sigma_0)^{max}_{meas}$ of the flood tide–oriented sand wave is 21%, respectively. The difference between $(\delta\sigma/\sigma_0)^{min}_{sim}$ and $(\delta\sigma/\sigma_0)^{min}_{meas}$ of the ebb tide–oriented sand wave is 10% and the difference between $(\delta\sigma/\sigma_0)^{min}_{sim}$ and $(\delta\sigma/\sigma_0)^{min}_{meas}$ of the flood tide–oriented sand wave is 43%, respectively. These results are acceptable but have to be improved.

[34] 4. The phases of simulated and measured NRCS modulations are correlated with the slopes of asymmetric sand waves. The phases of $(\delta\sigma/\sigma_0)^{max}_{sim}$ and $(\delta\sigma/\sigma_0)^{min}_{meas}$ of the ebb tide–oriented sand wave coincide fairly well; on the other hand only the phases of $(\delta\sigma/\sigma_0)^{min}_{sim}$ and $(\delta\sigma/\sigma_0)^{min}_{meas}$ of the flood tide–oriented sand wave coincide, where the phases between $(\delta\sigma/\sigma_0)^{max}_{sim}$ and $(\delta\sigma/\sigma_0)^{max}_{meas}$ show a difference in position of 15 m.

[35] 5. The magnitudes of the simulated and measured NRCS modulations of the ebb tide–oriented sand wave are significantly lower than the magnitudes of the flood tide–oriented sand wave. This is consistent with the theory because the strain rate is significantly lower for the ebb tide–oriented sand wave.

[36] **Acknowledgments.** For the management of the OROMA project we thank F. Ziemer as the responsible coordinator. The GKSS Research Center is gratefully acknowledged for use of their research facilities. G. Schymura, M. Cysewski, A. Bezuglov, I. Gorbunov, K. Prinz, and the captain and crew of the R/V *Ludwig Prandtl* are gratefully acknowledged for their excellent cooperation and assistance during the OROMA experiments. This work has been partially funded by the EU FP5 project OROMA, EVK3-CT-2001-00053.

References

Aliotta, S., and G. M. E. Perillo (1987), A sand wave field in the entrance to Bahia Blanca estuary, Argentina, *Mar. Geol.*, *76*, 1–14.

Alpers, W., and K. Hasselmann (1978), The two-frequency microwave technique for measuring ocean wave spectra from an airplane or satellite, *Boundary Layer Meteorol.*, *13*, 215–230.

Alpers, W., and I. Hennings (1984), A theory of the imaging mechanism of underwater bottom topography by real and synthetic aperture radar, *J. Geophys. Res.*, *89*, 10,529–10,546.

Bennett, S. J., and J. L. Best (1995), Mean flow and turbulence structure over fixed, two-dimensional dunes: Implications for sediment transport and bedform stability, *Sedimentology*, *42*, 491–513.

Calkoen, C. J., G. H. F. M. Hesselmans, G. J. Wensink, and J. Vogelzang (2001), The bathymetry assessment system: Efficient depth mapping in shallow seas using radar images, *Int. J. Remote Sens.*, *22*, 2973–2998.

Caponi, E. A., D. R. Crawford, H. C. Yuen, and P. G. Saffman (1988), Modulation of radar backscatter from the ocean by a variable surface current, *J. Geophys. Res.*, *93*, 12,249–12,263.

Coleman, J. M. (1969), Brahmaputra River: Channel processes and sedimentation, *Sediment. Geol.*, *3*, 129–239.

Cox, C., and W. Munk (1954), Measurement of the roughness of the sea surface from photographs of the sun glitter, *J. Opt. Soc. Am.*, *44*, 838–850.

De Loor, G. P. (1981), The observation of tidal patterns, currents and bathymetry with SLAR imagery of the sea, *IEEE J. Oceanic Eng.*, *6*, 124–129.

Donato, T. F., F. Askari, G. O. Marmorino, C. L. Trump, and D. R. Lyzenga (1997), Radar imaging of sand waves on the continental shelf east of Cape Hatteras, NC, U.S.A., *Cont. Shelf Res.*, *17*, 989–1004.

Ha, H. K., and S. K. Chough (2003), Intermittent turbulent events over sandy current ripples: A motion-picture analysis of flume experiments, *Sediment. Geol.*, *161*, 295–308.

Hennings, I. (1990), Radar imaging of submarine sand waves in tidal channels, *J. Geophys. Res.*, *95*, 9713–9721.
Hennings, I. (1998), An historical overview of radar imagery of sea bottom topography, *Int. J. Remote Sens.*, *19*, 1447–1454.
Hennings, I., H. Pasenau, and F. Werner (1993), Sea surface signatures related to subaqueous dunes detected by acoustic and radar sensors, *Cont. Shelf Res.*, *13*, 1023–1043.
Hennings, I., S. Stolte, and F. Ziemer (1994), Experimental method to measure surface signature generation by sea bottom undulations, *IEEE J. Oceanic Eng.*, *19*, 36–40.
Hennings, I., B. Lurin, and N. Didden (2001), Radar imaging mechanism of the sea bed: Results of the C-STAR experiment in 1996 with special emphasis on the relaxation rate of short waves due to current variations, *J. Phys. Oceanogr.*, *31*, 1807–1827.
Hennings, I., M. Metzner, and G.-P. De Loor (2002), The influence of quasi resonant internal waves on the radar imaging mechanism of shallow sea bottom topography, *Oceanol. Acta*, *25*, 87–99.
Hennings, I., D. Herbers, K. Prinz, and F. Ziemer (2004), First results of the OROMA experiment in the Lister Tief of the German Bight in the North Sea, *EARSeL eProc.*, *3*, 86–104.
Hesselmans, G. H. F. M., G. J. Wensink, C. G. Van Koppen, C. Vernemmen, and C. Van Cauwenberghe (2000), Bathymetry assessment demonstration off the Belgian coast—BABEL, *Hydrogr. J.*, *96*, 3–8.
Holliday, D., G. St-Cyr, and N. E. Woods (1986), A radar ocean imaging model for small to moderate incidence angles, *Int. J. Remote Sens.*, *7*, 1809–1834.
Hovanessian, S. A. (1980), *Introduction to Synthetic Array and Imaging Radars*, 156 pp., Artech House, Dedham, Mass.
Inglada, J., and R. Garello (2002), On rewriting the imaging mechanism of underwater bottom topography by synthetic aperture radar as a Volterra series expansion, *IEEE J. Oceanic Eng.*, *27*, 665–674.
Keller, G. H., and A. F. Richards (1967), Sediments of the Malacca Strait, southeast Asia, *J. Sediment. Petrol.*, *37*, 102–127.
Kostaschuk, R. A., and M. A. Church (1993), Macroturbulence generated by dunes: Fraser River, Canada, *Sediment. Geol.*, *85*, 25–37.
Lamont-Smith, T., A. M. Jackson, P. W. Shepherd, and R. D. Hill (2005), Low grazing angle radar imaging experiments over the South Falls sandbank, *Int. J. Remote Sens.*, *26*, 937–966.
Le Bot, S., and A. Trentesaux (2004), Types of internal structure and external morphology of submarine dunes under the influence of tide- and wind-driven processes (Dover Strait, northern France), *Mar. Geol.*, *211*, 143–168.
Li, X., J. Morrison, L. Pietrafesa, and A. Ochadlick (1999), Analysis of oceanic internal waves from airborne SAR images, *J. Coastal Res.*, *15*, 884–891.
Maddux, T. B., J. M. Nelson, and S. R. McLean (2003a), Turbulent flow over three-dimensional dunes: 1. Free surface and flow response, *J. Geophys. Res.*, *108*(F1), 6009, doi:10.1029/2003JF000017.
Maddux, T. B., S. R. McLean, and J. M. Nelson (2003b), Turbulent flow over three-dimensional dunes: 2. Fluid and bed stresses, *J. Geophys. Res.*, *108*(F1), 6010, doi:10.1029/2003JF000018.
Matthes, G. H. (1947), Macroturbulence in natural stream flow, *Eos Trans. AGU*, *28*, 255–262.
McLeish, W., D. J. P. Swift, R. B. Long, D. Ross, and G. Merrill (1981), Ocean surface patterns above sea-floor bedforms as recorded by radar, southern bight of North Sea, *Mar. Geol.*, *43*, M1–M8.
Nimmo Smith, W. A. M., S. A. Thorpe, and A. Graham (1999), Surface effects of bottom-generated turbulence in a shallow tidal sea, *Nature*, *400*, 251–254.
Phillips, O. M. (1977), *The Dynamics of the Upper Ocean*, 343 pp., Cambridge Univ. Press, New York.
Phillips, O. M. (1984), On the response of short ocean wave components at a fixed wavenumber to ocean current variations, *J. Phys. Oceanogr.*, *14*, 1425–1433.
Romeiser, R., and W. Alpers (1997), An improved composite surface model for the radar backscattering cross section of the ocean surface: 2. Model response to surface roughness variations and the radar imaging of underwater bottom topography, *J. Geophys. Res.*, *102*, 25,251–25,267.
Shuchman, R. A., D. R. Lyzenga, and G. A. Meadows (1985), Synthetic aperture radar imaging of ocean-bottom topography via tidal-currents interactions: Theory and observations, *Int. J. Remote Sens.*, *6*, 1179–1200.
Soulsby, R. L., R. Atkins, C. B. Waters, and N. Oliver (1991), Field measurements of suspended sediment over sandwaves, in *Sand Transport in Rivers, Estuaries and the Sea*, edited by R. Soulsby and R. Bettess, pp. 155–162, A.A. Balkema, Brookfield, Vt.
Stolte, S. (1990), Dynamics of short waves and wave breaking, *Rep. 1990-4*, 48 pp., Federal Armed Forces Underwater Acoust. and Mar. Geophys. Res. Inst., Kiel, Germany.
Tomiyasu, K. (1978), Tutorial review of synthetic-aperture radar (SAR) with applications to imaging of the ocean surface, *Proc. IEEE*, *66*, 563–583.
Ulrich, J., and H. Pasenau (1973), Morphologische Untersuchungen zum Problem der tidebedingten Sandbewegung im Lister Tief, *Küste*, *24*, 95–112.
Valenzuela, G. R. (1978), Theories for the interaction of electromagnetic and ocean waves—A review, *Boundary Layer Meteorol.*, *13*, 277–293.
Vogelzang, J. (1997), Mapping submarine sand waves with multiband imaging radar: 1. Model development and sensitivity analysis, *J. Geophys. Res.*, *102*, 1163–1181.
Vogelzang, J., G. J. Wensink, C. J. Calkoen, and M. W. E. Van der Kooij (1997), Mapping submarine sand waves with multiband imaging radar: 2. Experimental results and model comparison, *J. Geophys. Res.*, *102*, 1183–1192.
Zimmerman, J. F. T. (1985), Radar images of the sea bed, *Nature*, *314*, 224–226.

I. Hennings and D. Herbers, Leibniz-Institut für Meereswissenschaften an der Universität Kiel, Wischhofstrasse 1-3, D-24148 Kiel, Germany. (ihennings@ifm-geomar.de)